

# Microstructural Evolution and Oxidation Behavior of Alloy Ni-13Mo-13Cr-9W-3Fe-3Ti-2Al During Isothermal Exposure at 900 °C



HE JIANG, JIANXIN DONG, MAICANG ZHANG, and WEIMIN GUO

The microstructure evolution and oxidation behavior of alloy Ni-13Mo-13Cr-9W-3Fe-3Ti-2Al (alloy K4208), a newly developed Ni-Cr-W-Mo-based wear-resistant superalloy, were investigated by isothermal aging at 900 °C in air. Thermodynamic calculations, microstructure observations, electron probe microanalysis (EPMA), and precise microchemical analysis were used to study the microstructure evolution and oxidation mechanism of alloy K4208. The results showed that alloy K4208 was mainly composed of a P-like phase,  $M_6C$  (and  $M_{12}C$ ) carbide,  $\gamma'$  phase,  $\mu$  phase, and  $\gamma$  matrix. During the 900 °C aging, the  $\gamma'$  phase coarsened into irregular shapes, the  $M_6C$  (and  $M_{12}C$ ) carbide decomposed, and the  $\mu$  phase dissolved into the matrix, providing abundant Cr, Mo, and W for the growth of the P-like phase. Hence, the relationship between the different phases was established by element redistribution. In addition, the oxidation of alloy K4208 was a diffusion-controlled process, leading to the formation of a stable oxide layer composed of three parts: a thin layer of  $NiCr_2O_4$  spinel located on the outermost side, a continuous  $Cr_2O_3$  layer decorated with  $TiO_2$  in the middle, and an internal  $Al_2O_3$  layer.

<https://doi.org/10.1007/s11661-019-05336-4>

© The Minerals, Metals & Materials Society and ASM International 2019

## I. INTRODUCTION

ALLOY Ni-13Mo-13Cr-9W-3Fe-3Ti-2Al (alloy K4208) is a solution-strengthened cast superalloy designed in China. The nearest equivalent to this alloy is the ВЖЛ2-ВН alloy (Russia).<sup>[1]</sup> Alloy K4208 was developed as a wear-resistant nickel-based superalloy and can be used long-term at 800 °C in high-wear and high-corrosion environments. In addition, alloy K4208 can sustain short-term service temperatures of up to 1000 °C.<sup>[1]</sup> To achieve excellent wear resistance, alloy K4208 contains a large amount of alloying elements. The high concentrations of W and Mo are designed to provide strength at high temperatures.<sup>[2,3]</sup> Furthermore, since W can increase the diffusion activation energy and slow the diffusion process by strongly binding atoms, the addition of W can provide good heat resistance to the alloy.<sup>[4]</sup> Generally, the addition of Si is beneficial for improving the castability of alloy K4208 and provides a solution-strengthening effect. Generally, the Cr and Al

elements present in nickel-based superalloys can form an oxide surface layer that protects against degradation at high temperatures.<sup>[5]</sup>

The addition of alloying elements to alloy K4208 results in the alloy having good mechanical properties but complicates the phase evolution. To develop materials for high-temperature applications, a good understanding of the phase evolution that occurs during aging and high-temperature oxidation characterization is necessary to prevent various corrosion problems that occur at high temperatures.<sup>[6]</sup> The understanding of these processes facilitates a property and performance comparison, which aids in materials selection and the development of design guidelines for industrial applications.<sup>[7]</sup> Hence, a thorough understanding of the microstructure and phase evolution during the high-temperature aging of alloy K4208 is needed. It is generally accepted that carbides and topologically close-packed (TCP) phases are composed of Cr, Mo, W, and other refractory elements.<sup>[8]</sup> The combined amount of W, Cr, and Mo in the K4208 alloy is as high as 35 pct, providing great potential for the formation of TCP phases and carbides. However, until now, few reports have been published about the wear resistance behavior and castability of alloy K4208,<sup>[9]</sup> but studies on the microstructure and phase composition of this alloy have not been published. As a result, one aim of this work is to clarify the phase composition and

HE JIANG, JIANXIN DONG, and MAICANG ZHANG are with the School of Materials Science and Engineering, University of Science and Technology Beijing, Beijing 100083, China. Contact e-mail: jianghe17@sina.cn WEIMIN GUO is with the Central Iron & Steel Research Institute, Beijing, China.

Manuscript submitted December 20, 2018.

Article published online July 2, 2019

microstructure evolution of alloy K4208 during high-temperature aging.

Furthermore, high-temperature applications require that materials have excellent oxidation resistance.<sup>[10]</sup> The high-temperature oxidation resistance of materials is usually derived from the formation of a protective oxide layer, such as  $\text{Al}_2\text{O}_3$ <sup>[11]</sup> and  $\text{Cr}_2\text{O}_3$ .<sup>[12]</sup> However, the stoichiometries of the oxides that form vary with the chemical composition of the bulk alloy and the oxidation environment.<sup>[13,14]</sup> The oxidation behavior of nickel-based superalloys is complex due to the use of large amounts of alloying elements; the bulk alloy oxidizes, forming various oxides in various sequences.<sup>[15]</sup> Therefore, it is necessary to investigate the oxidation of alloy K4208 to determine how its oxidation behavior compares to different alloys, and information about the K4208 alloy is scarce.

Based on the abovementioned reasons, there is an urgent need to systematically understand the microstructure evolution and oxidation behavior of alloy K4208 during high-temperature exposures, which will provide a basis for further development and the application of alloy K4208 and related alloy systems. Since this alloy is designed to be used in the temperature range of 800 °C to 1000 °C, the isothermal exposure in this study was carried out at 900 °C. The surface and cross-sectional morphologies of the oxide layer were examined by scanning electron microscopy (SEM), and the compositions of the oxides were determined by energy dispersive X-ray spectroscopy (EDS) and X-ray diffraction (XRD). The phase evolution during aging was investigated by observing the microstructure and preparing a phase diagram. The results of this work can provide theoretical references for the microstructure stability and oxidation resistance of alloy K4208 during high-temperature isothermal exposures.

## II. EXPERIMENTAL MATERIAL AND PROCEDURE

The chemical composition of the K4208 alloy used in this study is listed in Table I. The material used in this work was manufactured by vacuum induction melting (VIM) and then remelted for investment casting to obtain a bar. The bar was solution treated at 1200 °C for 1 hour and aged at 870 °C for 3 hours. Samples with 12 mm diameters and 15 mm heights were sectioned from the bar, abraded with 800 grit SiC abrasive paper, and ultrasonically cleaned in ethanol to prepare for the isothermal exposure experiment.

**Table I. Chemical Composition of Alloy K4208 (Where the Compositions Are Represented as Wt Pct).**

C	Cr	W	Mo	Al	Ti	Fe	Si	B	Ni
0.15	13.44	8.98	13.62	2.28	2.58	3.06	.46	0.034	bal

The isothermal aging tests were carried out at 900 °C by a muffle furnace for different periods of time (5, 10, 20, 50, 100, 200, and 300 hours) to investigate the microstructure evolution and oxidation behavior of alloy K4208. The composition of the oxide layer was determined by a D/MAX-TTRIII X-ray diffractometer. Then, the samples were carefully abraded and mechanically polished to expose the cross-sectional structure of the oxide layer. Scanning electron microscopy (SEM) and energy dispersive spectroscopy (EDS) were used to observe the cross-sectional morphology and analyze the elemental distribution. A JSM-6510A scanning electron microscope equipped with EDS was used in this work.

Next, to prepare the samples for morphology observations, the samples were electrolytically polished with a solution of 20 pct  $\text{CH}_3\text{OH}$  and 80 pct  $\text{H}_2\text{SO}_4$  and then electrolytically etched with a solution containing 15 g  $\text{CrO}_3$ , 10 mL  $\text{H}_2\text{SO}_4$ , and 170 mL  $\text{H}_3\text{PO}_4$ . The evolution of the phases during aging was studied by field emission scanning electron microscopy (FESEM) and electron probe microanalysis (EPMA). FESEM was carried out on a Zeiss Ultra 55 field emission scanning electron microscope, and EPMA was performed by a JXA-7800F electron probe microanalyzer. The hardness of the sample was measured by an HB-3000B Brinell hardness tester. JMatPro commercial software was used to perform the thermodynamic calculation. The only input in the calculation was the alloy composition.

In addition, a more detailed phase analysis was carried out by microchemical phase analysis. The electrolytes used to separate the phases were selected based on Reference 16. The  $\gamma'$  precipitates were electrolytically extracted by an aqueous solution containing 10 g/L  $(\text{NH}_4)_2\text{SO}_4$  and 10 g/L  $\text{C}_6\text{H}_8\text{O}_7$  using a current density of 0.03  $\text{A}/\text{cm}^2$  at 15 °C to 20 °C. The carbides and the other phases were electrolytically extracted in a methanol solution containing 10 g/L KCl, 40 g/L  $\text{C}_7\text{H}_6\text{O}_6\text{S}$ , and 5 pct  $\text{C}_6\text{H}_8\text{O}_7$  using a current density of 0.05  $\text{A}/\text{cm}^2$  at  $-5$  °C to 0 °C. The extracted precipitates were then washed, dried, and collected for further determination. The crystallographic structures of the phases were determined by X-ray diffraction analysis using an X'Pert MPD X-ray diffractometer equipped with Cu  $K\alpha$  radiation. The chemical compositions of the phases were determined by inductively coupled plasma atomic emission spectrometry (ICP-AES) using an Optima 2100DV ICP-AES system.

## III. RESULTS

### A. Microstructure

A typical microstructure of the as-received K4208 alloy is shown in Figure 1, and the calculated results obtained by the JMatPro software are shown in Figure 2 for comparison. The microstructure shown in Figure 1(a) is characterized by large amounts of a plate-shaped phase. The EDS analysis shows that this phase is rich in Mo and W. The chemical compositions of the equilibrium phases calculated by the JMatPro software are summarized in Table II. There are two Mo-

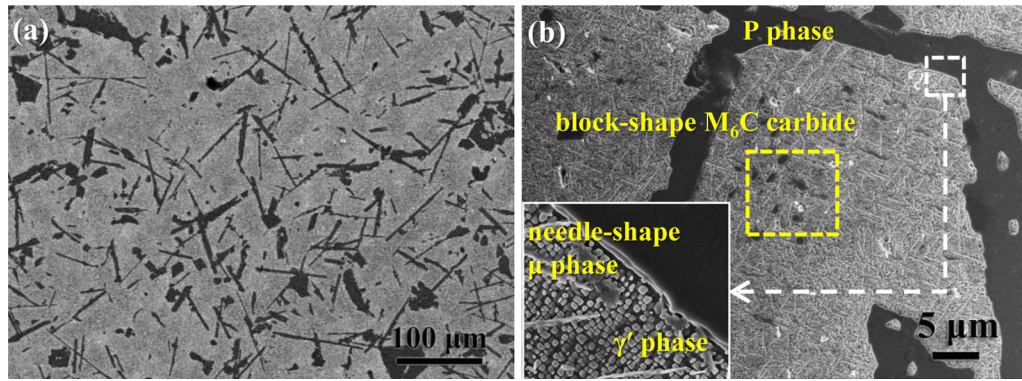


Fig. 1—Original microstructure of the as-received K4208 alloy: (a)  $\times 200$  magnification and (b)  $\times 5000$  magnification.

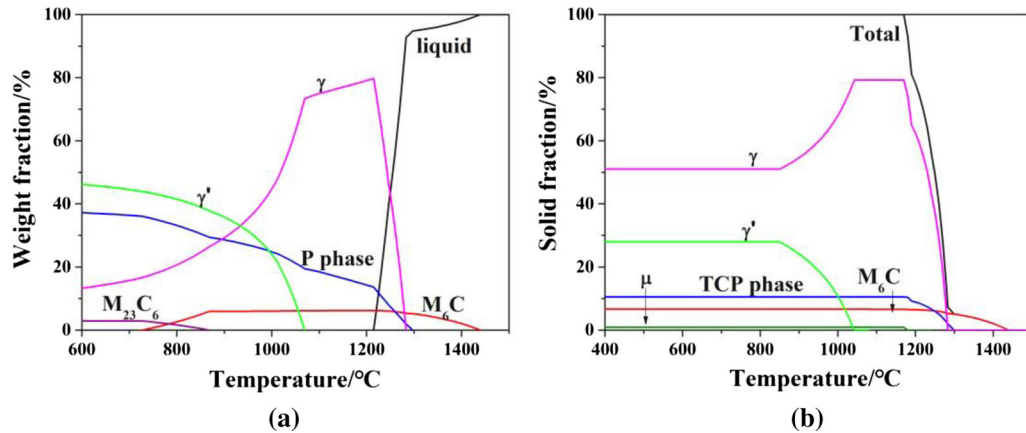


Fig. 2—Calculation results obtained by the JMatPro software: (a) property diagram calculated for alloy K4208 and (b) change in the solid fraction of the phases during solidification.

Table II. Chemical Composition of the Equilibrium Phases Calculated by JMatPro (Wt Pct)

	Cr	Mo	W	Fe	Ti	Al	Si	C	Ni
$\gamma$ Matrix	19.54	4.95	1.81	6.53	0.71	1.70	1.63	—	63.13
$\gamma'$	3.5	0.35	0.88	1.83	6.63	4.98	2.69	—	Bal
$M_6C$	14.42	44.48	12.97	2.8	—	—	0.48	2.52	Bal
$M_{23}C_6$	67.01	19.42	0.59	1.14	—	—	—	5.11	Bal
P Phase	19.34	31.83	25.75	1.15	—	—	—	—	Bal

and W-rich phases:  $M_6C$  carbides and the P phase. However, the  $M_6C$  carbide is depleted in Cr and rich in Si compared with the matrix. EPMA was used to obtain a more thorough understanding of the elemental distribution of the phases, as shown in Figure 3. The electron microprobe result further confirms that the large plate-shaped phase is rich in W and Mo, and the concentration of Cr in the plate-shaped phase is comparable with that in the  $\gamma$  matrix, which agrees with the result calculated for the P phase, which was obtained by JMatPro. The calculation results and elemental distribution results indicate that the P phase in alloy K4208 is partially composed of large Mo- and W-rich plates. Furthermore, the P phase is also composed of some particles that are depleted in Cr and rich in C. By combining these results with the results of the JMatPro

calculations, it can be deduced that these particles are  $M_6C$  carbides and have an intergrowth relationship with the P phase in alloy K4208. In addition, Figure 1(b) shows the morphologies of some round block particles in the matrix. The electron microprobe analysis and calculation results demonstrate that these particles are also  $M_6C$  carbides.  $M_6C$  carbides are one of the most common carbides observed in superalloys, and these carbides are usually rich in W and Mo and poor in Cr.<sup>[17]</sup> However, a Cr-rich  $M_6C$  carbide can form in Cr-rich superalloys during the solidification process,<sup>[18,19]</sup> as demonstrated by this study.

$\gamma'$  particles with diameters of approximately 200 nm are also distributed in the matrix. The  $\gamma'$  particles have rounded cubic shapes. Furthermore, some needle-like phases are also distributed throughout the matrix of

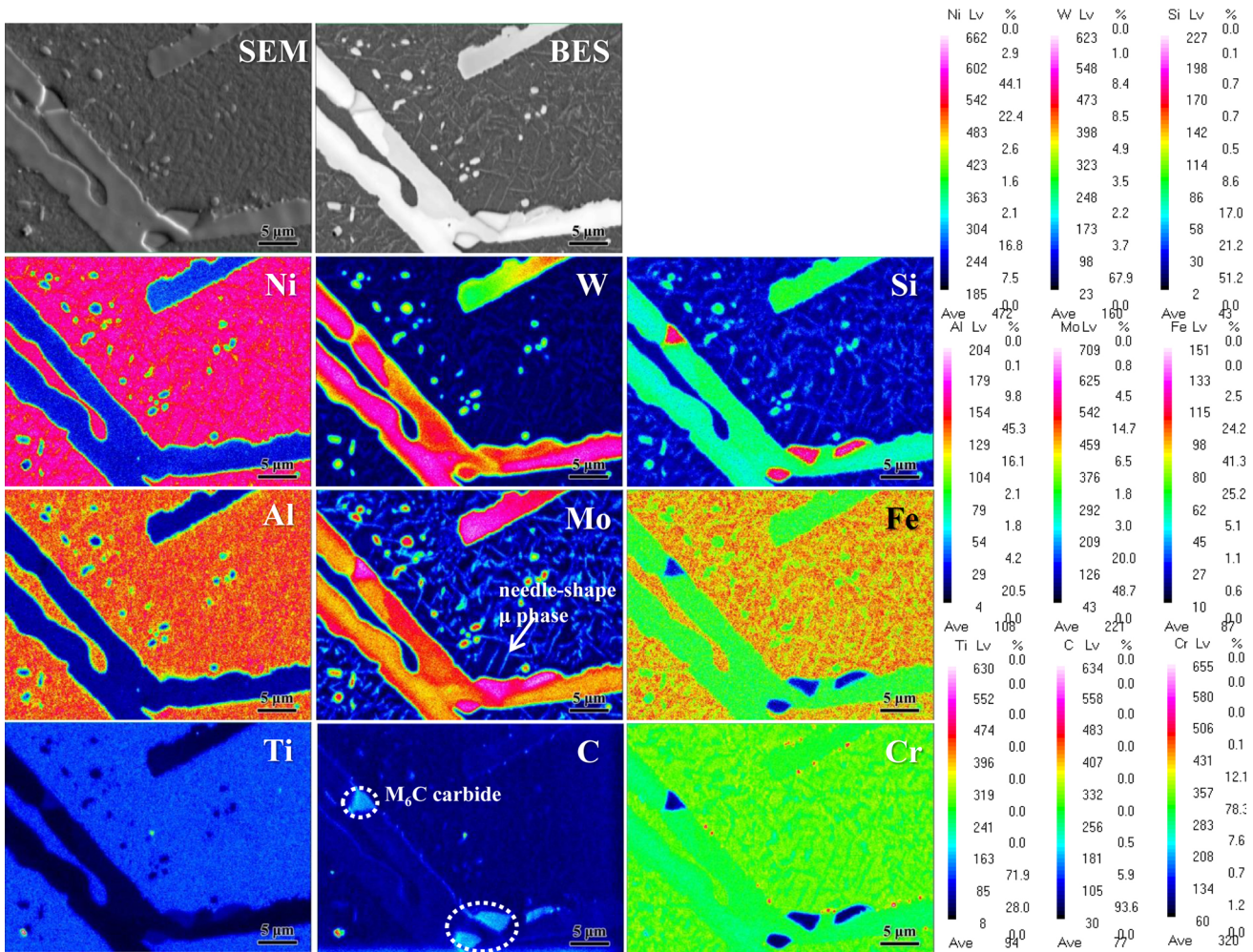


Fig. 3—Elemental distribution map for the as-received K4208 alloy, which was obtained by the electron microprobe analysis.

alloy K4208 (Figure 1(b)). The change in the solid fraction of the phases present in the alloy during solidification was calculated by JMatPro. Figure 2(b) shows that the  $\mu$  phase can form from a liquid in alloy K4208. This is a dynamic process and needs a driving force. The phase diagram for alloy K4208 (Figure 2(a)) only shows an equilibrium state. Therefore, the  $\mu$  phase is not achieved, as shown in Figure 2(a). Furthermore, investigations show that the stability of the  $\mu$  phase can be underestimated by calculated equilibrium phase diagrams.<sup>[20]</sup> It is generally accepted that W and Mo are  $\mu$ -phase-forming elements.<sup>[21]</sup> The high content of W and Mo in alloy K4208 facilitates the formation of the  $\mu$  phase. The abundance of Mo and W in the needle-shaped phase is also confirmed by the electron microprobe analysis, as shown in Figure 3. It is commonly accepted that the  $\mu$  phase precipitates during long thermal exposures.<sup>[22,23]</sup> However, when the content of refractory elements (such as Cr, Mo, W) is high enough and the content of W and Mo achieves a certain ratio, the  $\mu$  phase can precipitate as the primary phase in cast nickel-based superalloys.<sup>[24,25]</sup> The precipitation of the  $\mu$  phase is also reported in alloy K466 (which is another cast nickel-based superalloy with high W and Mo

contents).<sup>[23]</sup> Hence, it is reasonable that the  $\mu$  phase precipitates in alloy K4208, but the amount of the  $\mu$  phase is very limited in this case, as shown in Figures 1(b) and 2(b). The formation, evolution, and effect of the  $\mu$  phase in superalloys are complicated and strongly depend on the service environment<sup>[23,26]</sup> and variations in the concentrations of the  $\mu$ -forming elements (particularly Mo, W, and Fe).<sup>[27]</sup> The evolution of the  $\mu$  phase in alloy K4208 will be discussed in another manuscript and will not be analyzed in detail in this study.

To further investigate the phases present in alloy K4208, microchemical phase analysis was carried out. The  $\gamma'$  phase and  $M_6C$  carbide were detected, as shown in Figure 4 and Table III, which agrees with the abovementioned microstructure observations and calculation analyses. Another type of carbide is a  $M_{12}C$  carbide, which was detected in this study by microchemical phase analysis. However, this phase is not shown in the thermodynamic calculation, and the thermodynamic properties of the  $M_{12}C$  carbide are similar to those of the  $M_6C$  carbide. Therefore, the combined weight fractions of these two carbides were determined, as shown in Table III, and the individual

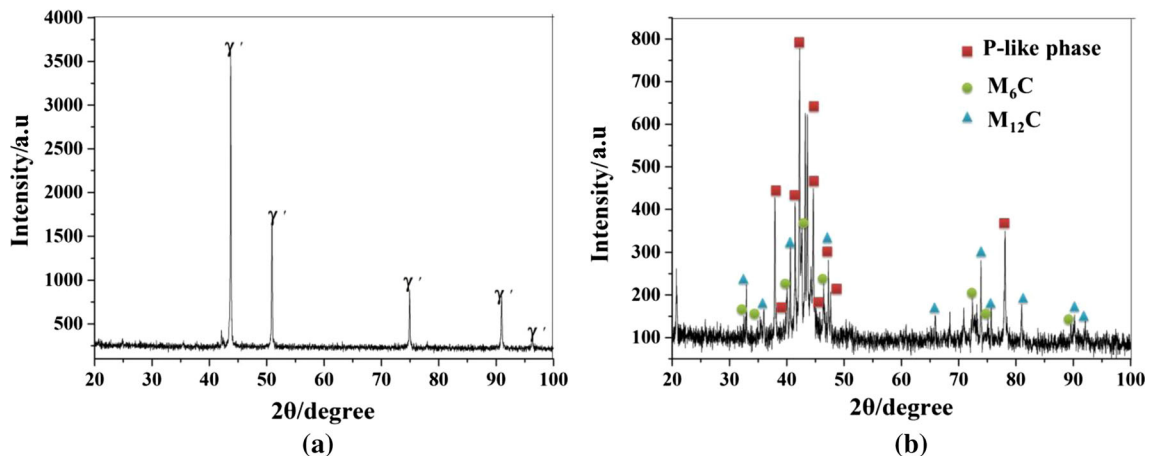


Fig. 4—XRD results of the phase determination during the microchemical phase analysis: (a)  $\gamma'$  phase and (b) P-like phase and carbides.

Table III. Microchemical Phase Analysis Results for the As-Received K4208 Alloy

Phase	Crystal System	Lattice Parameter (nm)	Chemical Formula	Weight Fraction (Pct)
$\gamma'$	face-centered cubic	$a_0 = 0.358$ to $0.359$	$\text{Ni}_{2.69}\text{Fe}_{0.04}\text{Cr}_{0.22}\text{W}_{0.12}\text{Mo}_{0.25}\text{Ti}_{0.29}\text{Al}_{0.38}$	19.14
$\text{M}_6\text{C}$	face-centered cubic	$a_0 = 1.100$ to $1.102$		8.075
$\text{M}_{12}\text{C}$	face-centered cubic	$a_0 = 1.086$ to $1.088$		
P-Like	orthorhombic	$a_0 = 0.8704$ $b_0 = 0.9898$ $c_0 = 0.4527$	$\text{Ni}_{0.348}\text{Fe}_{0.034}\text{Cr}_{0.215}\text{W}_{0.110}\text{Mo}_{0.281}\text{Ti}_{0.012}$	16.85

chemical formulas of the  $\text{M}_{12}\text{C}$  and  $\text{M}_6\text{C}$  carbides could not be determined. Generally, the chemical composition and crystal structure of the  $\text{M}_{12}\text{C}$  carbide is the same as that of the  $\text{M}_6\text{C}$  carbide present in superalloys, and the XRD patterns of both carbides are similar with only a slight difference in the  $d$  value. As a result, the  $\text{M}_{12}\text{C}$  carbide was previously referred to as a C-poor  $\text{M}_6\text{C}$  carbide.<sup>[28]</sup> The  $\text{M}_6\text{C}$  carbide and  $\text{M}_{12}\text{C}$  carbide were also identified in the GH3535 superalloy and can be stable for as long as 1000 hours at 800 °C.<sup>[29,30]</sup> This paper mainly focuses on the microstructure evolution and oxidation behavior of alloy K4208, and hence, in the following discussion, these two types of carbides are not distinguished and are referred to as the  $\text{M}_6\text{C}$  (and  $\text{M}_{12}\text{C}$ ) carbide.

Note that the XRD pattern obtained for the P phase does not completely agree with the patterned obtained from the Joint Committee on Powder Diffraction Standards (JCPDS) database. The detailed crystal structure information of the phases present in alloy K4208 is shown in Table III. Generally, the P phase (orthorhombic system,  $\text{oP}56$ ,  $a = 1.698$  nm,  $b = 0.475$  nm,  $c = 0.907$  nm)<sup>[31]</sup> is a TCP phase and can be detected in steel and sometimes in nickel-based alloys with extremely high Mo contents.<sup>[32,33]</sup> For example, the P phase is reported in Hastelloy C276 with 16.25 pct Mo.<sup>[34]</sup> Although the P phase has been researched,<sup>[20,35–37]</sup> detailed studies on the P phase are mainly limited to single-crystal superalloys. As a result, there are few references that can be used to determine the P phase, making the determination of the P phase difficult. Furthermore, superalloys are made using very

large amounts of alloying metals, which makes the phase composition complicated and variable. Based on the thermodynamic calculation, elemental distribution analysis and microchemical analysis, the large blocky phase detected in this work is referred to as a P-like phase in the following discussion.

The microchemical phase analysis shows that the weight fractions of the  $\gamma'$  phase and P-like phase are 19.14 pct and 16.85 pct, respectively. The chemical formula and lattice parameters of both phases in alloy K4208 were also determined, as shown in Table III. The  $\mu$  phase was not detected by the microchemical phase analysis, which may be attributed to the fact that the amount of the  $\mu$  phase is too small to be detected by such a method.

In summary, the microstructure observation, thermodynamic calculation, electron microprobe analysis, and microchemical phase analysis results together show that there are three main types of phases in alloy K4208. The large plate-shaped phase is a W- and Mo-rich P-like phase. There are also a number of  $\gamma'$  particles distributed in the  $\gamma$  matrix. Another major phase is a carbide that is rich in W and Mo and depleted in Cr. The following discussion of the microstructure evolution observed during aging will mainly focus on these phases.

## B. Microstructure Evolution During Isothermal Exposure

The microstructure evolution of alloy K4208 during aging at 900 °C is demonstrated in Figure 5. It can be concluded from Figure 5 that the amount of the P-like phase particles decreases slightly as the aging time is

prolonged, while the size simultaneously increases. In addition, the thickness of the P-like phase grows during aging (as illustrated by the blue dashed lines), which can be seen in the magnification of the microstructure shown in Figure 5(e), which was obtained after aging for 300 hours.

The morphology shown in Figure 5(b) illustrates that the edge of the  $M_6C$  (and  $M_{12}C$ ) carbide particle appears to be irregular after aging at 900 °C for 20 hours. The shape of the  $M_6C$  particle becomes more irregular as the aging progresses, as shown in Figures 5(c) and (d). The microstructure evolution of the  $M_6C$  (and  $M_{12}C$ ) carbide indicates that decomposition occurs during aging. Previous studies have shown that a  $M_6C$  carbide is unstable during thermal exposure and decomposes into a  $M_{23}C_6$  carbide in certain circumstances.<sup>[18,38–40]</sup> The stability of the  $M_6C$  carbide is related to the Cr concentration, and degeneration will occur when the Cr concentration is high enough.<sup>[18,39,40]</sup> An investigation of a Ni-Cr-W superalloy revealed that the Cr concentration in the  $M_6C$  carbide is up to 14.1 pct, and this leads to the instability of the  $M_6C$  carbide. The decomposition process of the  $M_6C$  carbide can be expressed as  $M_6C \rightarrow M_{23}C_6 + (W, Ni, Cr, Mo)$ , indicating that the  $M_{23}C_6$  carbide forms during the decomposition of the  $M_6C$  carbide, and large amounts of W, Mo, and Cr are released into the matrix.<sup>[41]</sup>

In addition, the needle-shaped  $\mu$  phase coarsens, and the shapes become irregular after 20 hours of aging. Studies have reported that, by prolonging the aging time, the needle-shaped  $\mu$  phase can dissolve and transform into block shapes to lower the interfacial energy.<sup>[23]</sup> The needle-shaped  $\mu$  phase cannot be detected after aging at 900 °C for 200 hours, as shown in Figure 5(d).

By comparing the enlarged microstructures shown in Figures 5(a) through (c), the size of the  $\gamma'$  phase increases with increasing aging time. Some of the  $\gamma'$  particles lose their rounded cubic shape and become irregularly shaped after 50 hours of aging (Figure 5(c)). The morphologies of most of the  $\gamma'$  particles become irregular when the aging time increases to 200 hours or more, as shown in Figures 5(d) and (e).

The elemental distribution map of alloy K4208 after 300 hours of aging, which was obtained by the electron microprobe analysis, is shown in Figure 6. The shapes of the phases shown in Figure 6 become irregular compared with Figure 3. Furthermore, the plate-shaped P-like phase coarsens significantly. The Al- and Ti-rich regions of the matrix contain  $\gamma'$  phase particles. The comparison of Figures 3 and 6 further confirms that the  $\gamma'$  particles coarsen during aging and their shapes become irregular, which agrees with the observations made from Figure 5.

The hardness evolution of alloy K4208 during aging is demonstrated in Figure 7. Figure 7 shows that the hardness of alloy K4208 is very high since it is a wear-resistant alloy. Furthermore, the hardness decreases with increasing aging time, indicating that the coarsening of the phase will cause the mechanical properties of alloy K4208 to deteriorate during aging at

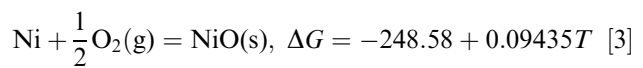
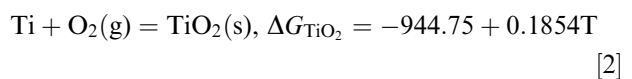
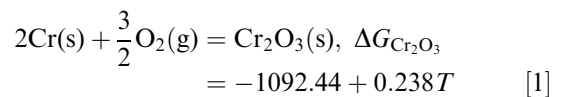
900 °C. However, the hardness of alloy K4208 still remains high.

### C. Oxidation Behavior

Oxidation resistance plays an important role in the evaluation of the high-temperature properties of alloys. The oxide scale did not spall during the isothermal exposure. The surface morphology of alloy K4208 after aging at 900 °C is shown in Figure 8, and the corresponding results of the EDS analysis performed on the oxide surface are summarized in Table IV. A thin Cr- and Ti-rich oxide layer covers the alloy surface after 5 hours of aging at 900 °C, as shown in Figure 8(a). The XRD analysis indicates that the Cr- and Ti-rich oxide layer is a mixture of  $Cr_2O_3$  and  $TiO_2$ , as shown in Figure 9, which agrees with the results of previous reports.<sup>[15,42]</sup> An alloy with a Cr/Al ratio (by weight) greater than 4 is referred to as a “chromia former,” according to the literature.<sup>[42]</sup> The Cr/Al ratio of alloy K4208 is 5.89, which classified alloy K4208 as a “chromia former.” Hence, it is reasonable that alloy K4208 has an oxide scale composed primarily of  $Cr_2O_3$ . In addition, the formation of  $TiO_2$  is possible since  $Ti^{4+}$  can diffuse through the  $Cr_2O_3$  layer.<sup>[15]</sup>

As the aging proceeds, a Cr-Ni-rich oxide with a spinel structure appears on the surface of the alloy after 50 hours of aging (Figure 8(b)). The EDS and XRD analyses confirm that this spinel oxide is a  $NiCr_2O_4$  spinel. The lattice diffusion coefficient of the Ni ions in the  $Cr_2O_3$  film is reportedly two times larger than that of the Cr ions.<sup>[43]</sup> Furthermore, oxidation is a diffusion-controlled process,<sup>[44]</sup> and Cr is consumed gradually as the oxide layer grows. Moreover, the concentration of Cr in alloy K4208 is relatively low, and oxidation results in the depletion of Cr in the subsurface. Hence, Ni is forced to participate in the oxidation process that occurs after longer aging times, owing to the high concentration of Ni in the alloy, which accelerates the formation of the Ni-rich  $NiCr_2O_4$  spinel.<sup>[45]</sup> The abundant Ni in the alloy facilitates the formation and growth of the  $NiCr_2O_4$  spinel, as shown in Figures 8(c) and (d). Such a  $NiCr_2O_4$  spinel can also be found in other common superalloys, such as Inconel 718,<sup>[6,45]</sup> Inconel 625,<sup>[46]</sup> and Inconel 740H,<sup>[44]</sup> during oxidation.

As alloy K4208 is exposed to a high-temperature environment, the following reactions can occur, based on the Ellingham–Richardson diagram<sup>[47–49]</sup>:



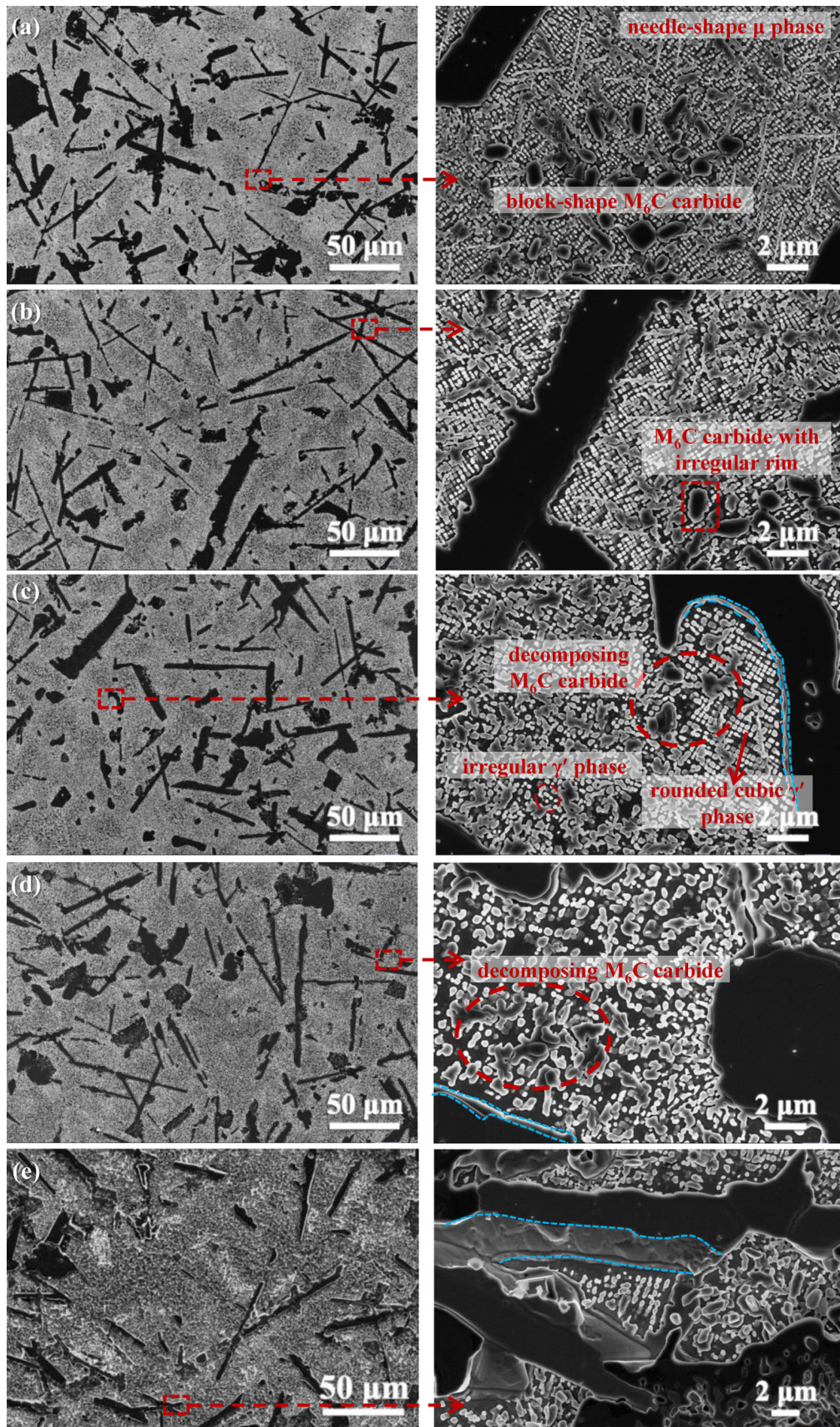


Fig. 5—Microstructure of alloy K4208 during aging at 900 °C for various lengths of time: (a) 5 h, (b) 20 h, (c) 50 h, (d) 200 h, and (e) 300 h.

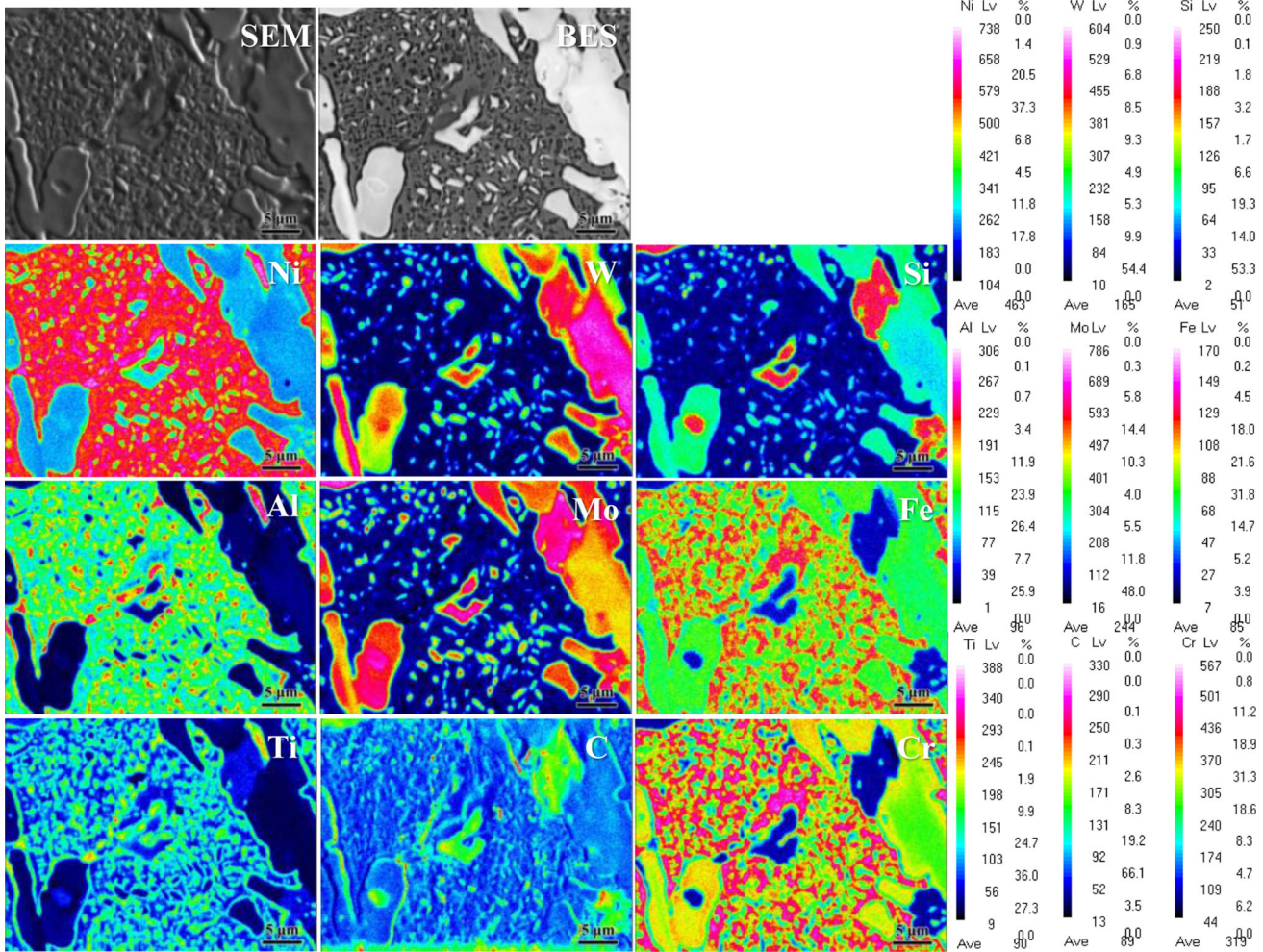


Fig. 6—Elemental distribution map for alloy K4208 after aging at 900 °C for 300 h, which was obtained by electron microprobe analysis.

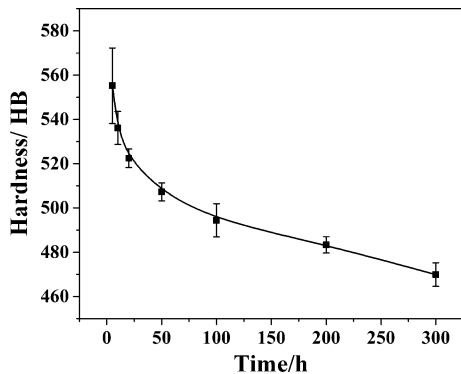
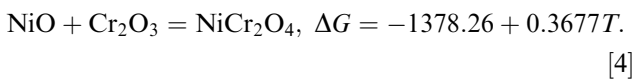


Fig. 7—Hardness evolution of alloy K4208 during aging at 900 °C.



Obviously, the above oxidation reactions can all occur spontaneously at 900 °C, because the corresponding Gibbs free energy values are negative.<sup>[45]</sup> It can be

concluded that the different thermodynamic stabilities of the oxides will drive the oxidation process.<sup>[50]</sup>

To study the oxidation behavior of alloy K4208, a cross-sectional morphology investigation was carried out. The backscattered electron (BSE) image obtained for the cross-sectional morphologies of alloy K4208 after aging at 900 °C is illustrated in Figure 10. The oxide layer is composed of external (light gray) and internal (dark gray) layers. The composition and evolution of the external layer has been discussed in detail in the abovementioned surface morphology section. An internal oxide layer forms, indicating that O can penetrate the matrix. In this condition, O penetrates the matrix either by traveling through the oxide scale and metal or adsorbing to the alloy surface during the early stages of aging or prior to oxidation.<sup>[44]</sup> The EDS analysis indicates that the internal oxide layer is mainly composed of island-shaped Al<sub>2</sub>O<sub>3</sub>. Al<sub>2</sub>O<sub>3</sub> is a common internal oxide detected in superalloys,<sup>[6,10]</sup> because it has high thermodynamic stability and is able to form at the lowest oxygen partial pressure compared to other oxides.<sup>[15,51]</sup> Furthermore, as previously discussed, alloy K4208 is classified as a “chromia former,” due to its Cr and Al content. This means that the steady-state



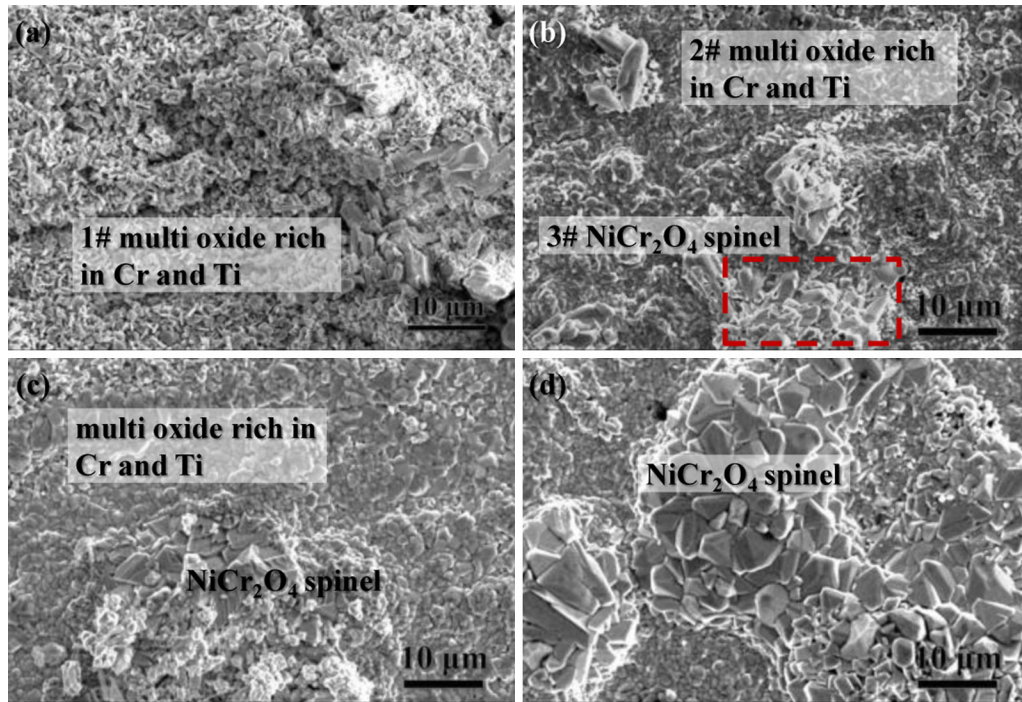


Fig. 8—Surface morphology of alloy K4208 after aging at 900 °C for (a) 5 h, (b) 50 h, (c) 100 h, and (d) 300 h.

**Table IV. EDS Analysis Results for a Typical Composition of Alloy K4208 Oxides, as Shown in Fig. 5**

	O	Al	Ti	Cr	Ni	Mo	W
1#	25.25	2.99	11.42	35.12	23.88	0.17	1.07
2#	30.78	1.47	14.00	27.11	25.62	0.11	0.91
3#	24.03	0.11	1.19	45.89	28.45	—	0.33

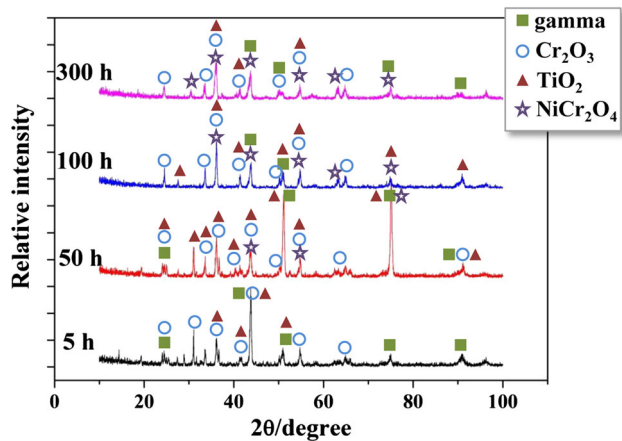


Fig. 9—XRD analysis results obtained for the oxide scale that formed on alloy K4208 after aging at 900 °C for different periods of time.

oxidation is characterized by the slow growth of a dense  $\text{Cr}_2\text{O}_3$  film and the internal oxidation of Al,<sup>[6]</sup> as shown in this work. With increasing aging time,  $\text{Al}_2\text{O}_3$  grows

deeper into the matrix and becomes coarser, as shown in Figure 10, indicating that O continuously diffuses into the matrix. In addition, when the aging time increases to 200 hours, a spinel oxide layer can be found on the outermost oxide layer, as marked in Figure 10(c). This agrees with the abovementioned analysis, which indicated that the continuous outer diffusion of Ni accelerates the formation of the  $\text{NiCr}_2\text{O}_4$  spinel.

The elemental distribution maps obtained by EDS provide a more direct understanding of the elemental diffusion trend observed during oxidation, as demonstrated in Figure 11. Ti accumulates on the outer layer after the alloy was aged at 900 °C for 10 hours (Figure 11(a)), and this is more apparent after the aging time is increased up to 100 hours (Figure 11(b)). The accumulation of Ti can be observed both at the matrix/oxide interface and on the surface of the external oxide. Ti accumulates due to the outward diffusion of  $\text{Ti}^{4+}$ . A similar phenomenon was also reported for Haynes 282<sup>[15]</sup> and Inconel 740.<sup>[52]</sup> The diffusion rate of  $\text{Ti}^{4+}$  was shown to be greater than that of  $\text{Cr}^{3+}$ <sup>[53]</sup> Furthermore, Ti has a high affinity for oxygen,<sup>[52]</sup> and the formation of  $\text{TiO}_2$  is more thermodynamically favored than the formation of  $\text{Cr}_2\text{O}_3$ .<sup>[15]</sup> As the aging time is prolonged, the accumulation of Ti is more apparent in the outermost oxide layer, as shown in Figure 11(b). The external oxide layer is a mixture of  $\text{Cr}_2\text{O}_3$  and  $\text{TiO}_2$ . In addition, the accumulation of Al beneath the external oxide layer/matrix interface is more apparent with increasing aging time. This agrees with the morphology analysis shown in Figure 10, which shows that the internal oxidation is becoming more obvious.

The effect of aging time on the growth of the oxide layer is summarized in Figure 12. The thicknesses of

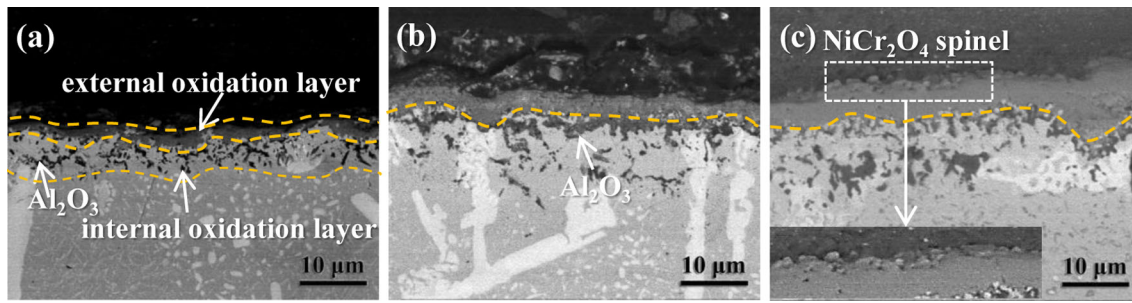


Fig. 10—BES images showing the cross-sectional morphologies of the oxide on the alloy surface when alloy K4208 was aged at 900 °C for (a) 5 h, (b) 20 h, and (c) 200 h.

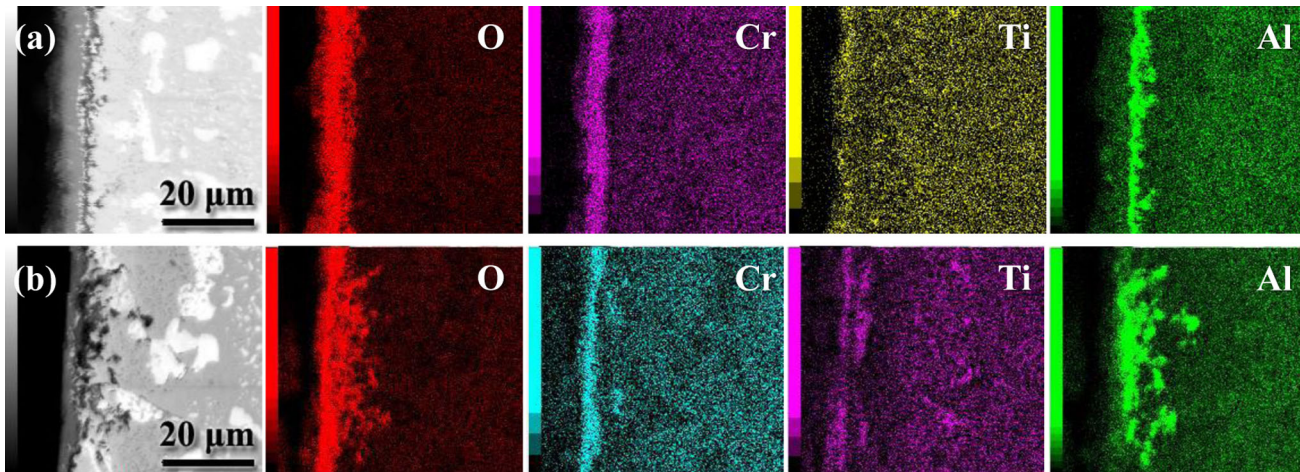


Fig. 11—Elemental distribution of alloy K4208 after aging at 900 °C for (a) 10 h and (b) 100 h.

both the internal and external oxide layers increase with increasing aging time, which agrees with the results shown in Figure 10. The increasing rate of the oxide layer formation slows down as the aging proceeds. This occurs because, after the formation of a continuous external oxide layer, the growth of the oxide layer is controlled by the migration of metallic elements from the base metal and the penetration of O into the matrix.<sup>[44]</sup> In this condition, the increase in the oxide layer thickness with increasing time is parabolic.<sup>[54]</sup> In addition, a previous study confirms that the formation of TiO<sub>2</sub> on the metal/oxide interface can retard the diffusion of Cr and O through the oxide scales, causing the oxidation rate to slow.<sup>[52]</sup>

## IV. DISCUSSION

### A. Phase Transformation Mechanism

The abovementioned experiments and analyses confirm that the major phases present in alloy K4208 are the Mo-W-rich P-like phase, a Mo-W-rich carbide (including the M<sub>6</sub>C-type and M<sub>12</sub>C-type carbides), and the γ' phase. The γ' phase coarsens rapidly during aging, and in this process, Cr and Mo are released from the γ' phase into the matrix.<sup>[55]</sup> The coarsening of the TCP phases and carbides are both diffusion-controlled processes.<sup>[8]</sup>

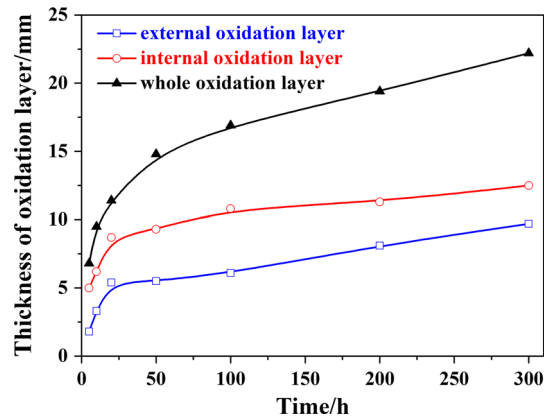


Fig. 12—Influence of time and temperature on the thickness of the oxide layer of alloy K4208. The solid line indicates the influence of time, and the dashed line indicates the influence of temperature.

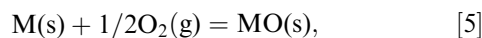
The JMatPro calculation results and morphology observation results confirm that the P-like phase in alloy K4208 is stable during aging, while the μ phase dissolves gradually. The μ phase is also a W-Mo-rich TCP phase, and the dissolution of the μ phase will release refractory elements into the matrix. Hence, it is reasonable to assume that the dissolution of the μ phase benefits the growth of the P-like phase by supplying refractory

elements. The intergrowth of the P phase and the  $\mu$  phase in a Ru-containing single-crystal superalloy is reported by Tan *et al.*, and in this work, the P phase grows by consuming the  $\mu$  phase.<sup>[56]</sup> Furthermore, the Cr and Mo elements released by the  $\gamma'$  phase can also transfer into the P-like phase through the matrix to facilitate growth. In addition, the  $M_6C$  (and  $M_{12}C$ ) carbide in alloy K4208 is not stable during aging, as shown in Figure 5. Large amounts of W, Mo, and Cr can be released into the matrix during the decomposition of the  $M_6C$  (and  $M_{12}C$ ) carbide.

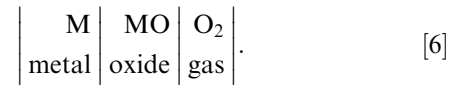
Based on the abovementioned discussion, the elemental diffusion-controlled phase evolution process can be summarized by the schematic diagram shown in Figure 13. Due to the thermal exposure, the initially rounded square  $\gamma'$  phase coarsens gradually, and some of the shapes of the  $\gamma'$  phase particles become irregular. During this process, Cr and Mo are released from the  $\gamma'$  phase into the matrix. At the same time, the  $M_6C$  (and  $M_{12}C$ ) carbide decomposes and releases W, Cr, and Mo. The needle-shaped  $\mu$  phase slowly dissolves into the matrix during aging, which results in the accumulation of W and Mo in the matrix. The evolution of the  $\gamma'$  phase, carbide, and  $\mu$  phase during aging leads to the accumulation of the refractory elements (W, Cr, and Mo) in the matrix. The adequate supply of W, Cr, and Mo facilitates the growth of the P-like phase, and these elements transfer into the P-like phase in this process.

### B. Oxidation Mechanism

Based on the abovementioned discussion concerning the oxidation behavior, it can be concluded that the oxidation of alloy K4208 is also a diffusion-controlled process. The oxidation of alloy K4208 and a typical cross-sectional oxidation morphology are shown in Figure 14. The oxidation of a pure metal can be represented by the following equation<sup>[57]</sup>:



where the two major reactants M and O are separated by the solid reaction product MO in the following way:



Hence, to drive the reaction, the reactants must pass through the oxide film, and this is an important part of the high-temperature oxidation mechanism.<sup>[58]</sup> The elements travel through the oxide layer in the form of electrons and ions. Therefore, either an excess or a deficit of metal ions (or either a deficit or an excess of oxygen) always exists in the oxide layer, which results in the charge difference in the oxide and drives the transport of the elements.<sup>[57]</sup>

In the initial stage of oxidation, oxygen molecules are absorbed onto the alloy surface,  $Cr^{3+}$  diffuses outward toward the matrix, and  $Cr_2O_3$  forms on the alloy surface. This occurs because the diffusion rate of  $Cr^{3+}$  is 2 to 3 times faster than that of  $O^{2-}$ .<sup>[10]</sup> At the same time,  $Ti^{4+}$ , which initially has the highest mobility, also diffuses quickly toward the metal/gas interface to form  $TiO_2$ . However, since there is less Ti in alloy K4208 compared to Cr, the formation of  $TiO_2$  is limited. A continuous oxide layer mainly composed of  $Cr_2O_3$  and decorated by  $TiO_2$  gradually forms, as demonstrated in Figure 11. The external oxide layer grows from the matrix and forms on the gas side. A previous study has also confirmed that metal-deficient oxides, such as Ni, Cr, and Ti oxides, grow outward by the outward diffusion of metal cations, which react with O at the oxide/gas interface.<sup>[59]</sup> After the continuous external oxide layer forms, O must penetrate the oxide layer to get to the oxide/metal interface, and as a result, oxidation starts to be controlled by the inward diffusion of O and the outward diffusion of Cr,<sup>[49]</sup> causing the oxidation rate to slow.

Meanwhile, O penetrates the matrix to react with Al, which results in the formation of  $Al_2O_3$ . As the aging proceeds, the  $Al_2O_3$  layer grows deeper into the matrix to form an internal  $Al_2O_3$  layer, as indicated in Figure 11. This agrees with the report that oxygen-deficient oxides, such as Al, W, and Ta oxides, grow inward from the surface into the matrix by the diffusion of  $O^{2-}$ , which reacts with metal cations.<sup>[60]</sup> The lattice diffusion coefficient and grain boundary diffusion coefficient of oxygen in polycrystalline  $Cr_2O_3$  at 900 °C are

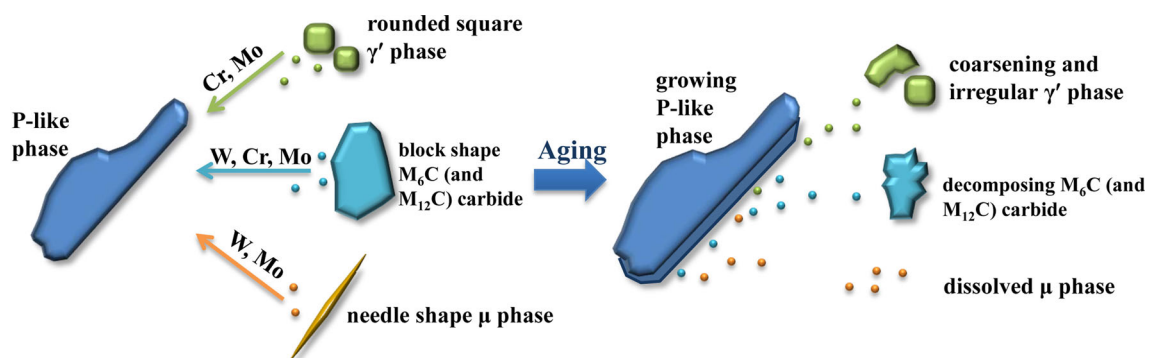


Fig. 13—Schematic diagram illustrating the phase evolution process for alloy K4208.

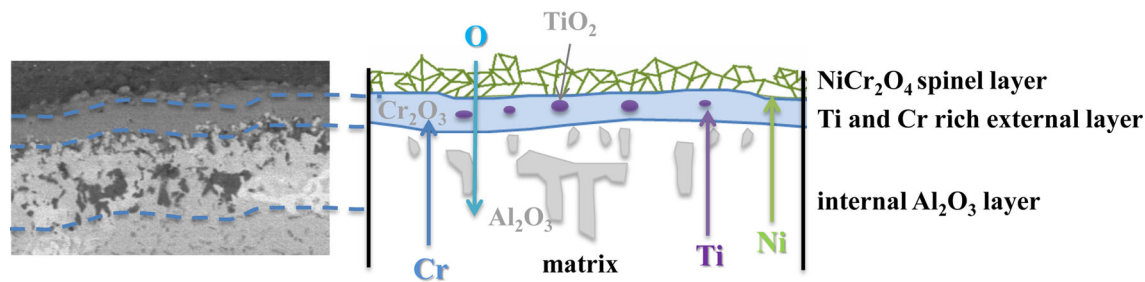


Fig. 14—Schematic diagram illustrating the oxidation of alloy K4208.

$7.4 \times 10^{-16}$  to  $8.1 \times 10^{-16}$  and  $1.6 \times 10^{-16}$  to  $4.3 \times 10^{-16} \text{ cm}^2 \text{ s}^{-1}$ , respectively.<sup>[61]</sup> Furthermore, the continuous reaction that occurs in the external oxide layer results in the depletion of Cr on the surface, while the concentration of Ni increases due to the outward diffusion. Therefore, Ni participates in the reaction, leading to the formation of the  $\text{NiCr}_2\text{O}_4$  spinel on the outermost layer. It is reported that the bulk diffusion coefficients of Cr and Ni in a  $\text{Cr}_2\text{O}_3$  film at  $900^\circ\text{C}$  are  $8 \times 10^{-16}$  and  $4 \times 10^{-16} \text{ cm}^2 \text{ s}^{-1}$ , respectively. The grain boundary diffusion coefficients of these two elements in a  $\text{Cr}_2\text{O}_3$  film at  $900^\circ\text{C}$  are  $5 \times 10^{-11}$  and  $1 \times 10^{-12} \text{ cm}^2 \text{ s}^{-1}$ , respectively.<sup>[62]</sup> Though the value obtained in this work differs from that of Reference 43, the diffusion rate of Ni is typically slightly higher than that of Cr. Hence, Ni can diffuse through the  $\text{Cr}_2\text{O}_3$  film to the oxide/air interface to form the  $\text{NiCr}_2\text{O}_4$  spinel layer. A typical cross-sectional oxide layer is composed of three parts: a thin layer of a  $\text{NiCr}_2\text{O}_4$  spinel on the outermost side, a continuous Ti- and Cr-rich external layer in the middle and an internal  $\text{Al}_2\text{O}_3$  layer.

## V. CONCLUSION

In this work, the microstructure evolution and oxidation behavior of alloy K4208 during aging are investigated by an isothermal exposure at  $900^\circ\text{C}$ . Based on the discussion and analyses, the following conclusions were obtained:

1. The major phases present in alloy K4208 are the P-like phase,  $\text{M}_6\text{C}$  (and  $\text{M}_{12}\text{C}$ ) carbide,  $\gamma'$  phase, and  $\mu$  phase. During aging, the  $\mu$  phase is not stable and gradually dissolves into the matrix, while the  $\gamma'$  phase coarsens into irregular shapes. Meanwhile, the  $\text{M}_6\text{C}$  (and  $\text{M}_{12}\text{C}$ ) carbide decomposes. These phase evolution processes release Cr, Mo, and W into the matrix, which benefits the growth of the P-like phase.
2. The oxidation behavior of alloy K4208 during the  $900^\circ\text{C}$  aging is a diffusion-controlled process. A complex layer containing  $\text{Cr}_2\text{O}_3$  and  $\text{TiO}_2$  initially forms during the early stages of oxidation. Afterward, O penetrates the matrix to react with Al, forming the  $\text{Al}_2\text{O}_3$  internal oxide layer. The outward diffusion of Ni leads to the formation of the  $\text{NiCr}_2\text{O}_4$  spinel on the outermost layer. As a result,

the oxide layer is composed of three parts: a thin layer of a  $\text{NiCr}_2\text{O}_4$  spinel on the outermost side, a continuous Ti- and Cr-rich external layer in the middle, and an internal  $\text{Al}_2\text{O}_3$  layer.

## ACKNOWLEDGMENTS

The authors appreciate the financial support provided by the National Natural Science Foundation of China under Grant No. 51701011 and the Fundamental Research Funds for the Central Universities under Grant No. FRF-TP-17-002A1. And special thanks to Prof. Weimin Guo (Central Iron & Steel Research Institute) for the contribution in this work.

## REFERENCES

1. CMS Academic Committee of the Superalloys: *China Superalloys Handbook*, China Standards Press, Beijing, 2012.
2. D.W. Yun, S.M. Seo, H.W. Jeong, I.S. Kim, and Y.S. Yoo: *J. Alloys Compd.*, 2014, vol. 587, pp. 105–112.
3. D.W. Yun, S.M. Seo, H.W. Jeong, and Y.S. Yoo: *J. Alloys Compd.*, 2017, vol. 710, pp. 8–19.
4. Y. Zhang, X. Hu, C. Li, W. Xu, and Y. Zhao: *Mater. Des.*, 2017, vol. 129, pp. 26–33.
5. A. Kewther, M.S.J. Hashmi, and B.S. Yilbas: *J. Mater. Eng. Perform.*, 2001, vol. 10, pp. 108–113.
6. Kh.A. Al-Hatab, M.A. Al-Bukhaiti, U. Krupp, and M. Kantehm: *Oxid. Met.*, 2011, vol. 75, pp. 209–228.
7. M.S. Pampana: in *The Department of Mechanical Engineering*, Louisiana State University, Louisiana, 2004.
8. J. Liu, J. Li, F.S. Hage, P. Ghosh, J. Li, W. Wang, Z. Chen, T. Wang, W. Tang, and Q. Ramasse: *Acta Mater.*, 2017, vol. 131, pp. 169–86.
9. W. Guo, M. Zhao, J. Wu, J. Zhao, and Z. Chen: in *11th Chinese Superalloy Conference*, 2007, pp. 368–71.
10. J. Cao, J. Zhang, R. Chen, Y. Ye, and Y. Hua: *Mater. Charact.*, 2016, vol. 118, pp. 122–28.
11. X.H. Wang and Y.C. Zhou: *Oxid. Met.*, 2003, vol. 59, pp. 303–320.
12. Y. Hua, Z. Rong, Y. Ye, K. Chen, R. Chen, Q. Xue, and H. Liu: *Appl. Surf. Sci.*, 2015, vol. 330, pp. 439–44.
13. T.-H. Kim, D.-H. Lee, D. Kim, C. Jang, and J.-I. Yun: *J. Anal. At. Spectrom.*, 2012, vol. 27, pp. 1525–31.
14. J.H. Chen, P.M. Rogers, and J.A. Little: *Oxid. Met.*, 1997, vol. 47, pp. 381–410.
15. F.A. Pérez-González, N.F. Garza-Montes-de Oca, and R. Colás: *Oxid. Met.*, 2014, vol. 82, pp. 145–61.
16. *The Physicochemical Phase Analysis in Steel, Iron and Nickel-Base Alloy*, Shanghai University of Science and Technology Press, Shanghai, 1981.

17. M.M. Chiavaras, J.A. Jacobson, R. Carlos, E. Maida, T. Bentley, N. Simunovic, M. Swinton, and M. Bhandari: *Mater. Sci. Eng., A*, 2008, vol. 485, pp. 74–79.
18. B. Djerdjare, S. Lebaili, and S. Lay: *Mater. Sci. Eng., A*, 2008, vol. 475, pp. 336–42.
19. S.H. Zangeneh and H. Farhangi: *Mater. Des.*, 2010, vol. 31, pp. 3504–11.
20. C.M.F. Rae, M.S.A. Karunaratne, C.J. Small, R.W. Broomfield, C.N. Jones, and R.C. Reed: in *Superalloys 2000: Proceedings of the Ninth International Symposium on Superalloys*, ed. T.M. Pollock, TMS, Pennsylvania, 2000, pp. 767–76.
21. W. Sun, X. Qin, J. Guo, L. Lou, and L. Zhou: *Acta Metall. Sin.*, 2015, vol. 51, pp. 67–76.
22. R. Krishna, S.V. Hainsworth, S.P.A. Gill, A. Strang, and H.V. Atkinson: *Metall. Mater. Trans. A*, 2013, vol. 44A, pp. 1419–29.
23. X.Z. Qin, J.T. Guo, C. Yuan, G.X. Yang, L.Z. Zhou, and H.Q. Ye: *J. Mater. Sci.*, 2009, vol. 44, pp. 4840–47.
24. C.M.F. Rae and R.C. Reed: *Acta Mater.*, 2001, vol. 49, pp. 4113–25.
25. Y. Zheng: *Acta Metall. Sin.*, 1999, vol. 35, pp. 1242–45.
26. J.X. Yang, Q. Zheng, X.F. Sun, H.R. Guan, and Z.Q. Hu: *Scripta Mater.*, 2006, vol. 55, pp. 331–34.
27. H.M. Tawancy: *J. Mater. Sci.*, 1996, vol. 31, pp. 3929–3936.
28. L. Jinsheng: *Common Phases Identification Manuals for Steel and Alloys by X-ray*, Central Iron & Steel Research Institute, Beijing, 1990.
29. F. Han, L. Jiang, X. Ye, Y. Lu, Z. Li, and X. Zhou: *Materials*, 2017, vol. 10, p. 521.
30. T. Liu, J.S. Dong, L. Wang, Z.J. Li, X.T. Zhou, L.H. Lou, and J. Zhang: *J. Mater. Sci. Technol.*, 2015, vol. 31, pp. 269–79.
31. P. Villars and L.D. Calvert: *Pearson's Handbook of Crystallographic Data for Intermetallic Phases*, American Society of Metals, Cleveland, OH, 1985.
32. J. Huo, Q. Shi, Y. Zheng, and Q. Feng: *Mater. Charact.*, 2017, vol. 124, pp. 73–82.
33. Kexin. Guo: *Acta Metall. Sin.*, 1978, vol. 14, pp. 73–95.
34. R.B. Leonard: *Corrosion*, 1969, vol. 25, pp. 222–32.
35. R. Darolia, D.F. Lahrman, and R.D. Field: in: *Superalloys 1988: Proceedings of the Sixth International Symposium on Superalloys*, The Metallurgical Society of AIME, Pennsylvania, 1988, pp. 255–64.
36. R.A. Hobbs, L. Zhang, C.M.F. Rae, and S. Tin: *Metall. Mater. Trans. A*, 2008, vol. 39A, pp. 1014–25.
37. K. Hiraga, T. Yamamoto, and M. Hirabayashi: *Trans. Jpn. Inst. Met.*, 1983, vol. 24, pp. 421–28.
38. S. Hamar-Thibault, M. Durand-Charre, and B. Andries: *Metall. Trans. A*, 1982, vol. 13A, pp. 545–50.
39. G.V. Prasad Reddy, P. Harini, R. Sandhya, K. Bhanu Sankara Rao, and R.K. Paretkar: *Mater. Sci. Eng. A*, 2010, vol. 527, pp. 3848–51.
40. S. Chomette, J.-M. Gentzmittel, and B. Viguier: *J. Nucl. Mater.*, 2010, vol. 399, pp. 266–74.
41. G. Bai, J. Li, R. Hu, T. Zhang, H. Kou, and H. Fu: *Mater. Sci. Eng., A*, 2011, vol. 528, pp. 2339–44.
42. F.J. Liu, M.C. Zhang, J.X. Dong, and Y.W. Zhang: *Acta Metall. Sin. Engl.*, 2007, vol. 20, pp. 102–10.
43. R.E. Lobnig, H.P. Schmidt, K. Hennesen, and H.J. Grabke: *Oxid. Met.*, 1992, vol. 37, pp. 81–93.
44. H. Jiang, J. Dong, M. Zhang, L. Zheng, and Z. Yao: *Oxid. Met.*, 2015, vol. 84, pp. 61–72.
45. Q. Jia and D. Gu: *Opt. Laser Technol.*, 2014, vol. 62, pp. 161–71.
46. A. Vesel, A. Drenik, K. Elersic, M. Mozetic, J. Kovac, T. Gyergyek, J. Stockel, J. Varju, R. Panek, and M. Balat-Pichelin: *Appl. Surf. Sci.*, 2014, vol. 305, pp. 674–682.
47. C.V. Robino: *Metall. Mater. Trans. B*, 1996, vol. 27B, pp. 65–69.
48. Q. Pang, G.H. Wu, Z.Y. Xiu, L.T. Jiang, and D.L. Sun: *Mater. Charact.*, 2012, vol. 70, pp. 125–36.
49. L. Zheng, M. Zhang, and J. Dong: *Appl. Surf. Sci.*, 2010, vol. 256, pp. 7510–15.
50. W. Wei, H. Wang, C. Zou, Z. Zhu, and Z. Wei: *Mater. Des.*, 2013, vol. 46, pp. 1–7.
51. P. Berthod, S. Michon, J. Di Martino, S. Mathieu, S. Noël, R. Podor, and C. Rapin: *Calphad*, 2003, vol. 27, pp. 279–88.
52. S. Zhao, X. Xie, and G.D. Smith: *Surf. Coat. Technol.*, 2004, vol. 185, pp. 178–83.
53. S. Zhang, Q. Wang, X. Zhao, and C. Zhang: *J. Shenyang Univ. Technol.*, 2010, vol. 32, pp. 136–40.
54. X.-M. Hou and K.-C. Chou: *J. Eur. Ceram. Soc.*, 2009, vol. 29, pp. 517–23.
55. J.S. Hou and J.T. Guo: *J. Mater. Eng. Perform.*, 2006, vol. 15, pp. 67–75.
56. X.P. Tan, J.L. Liu, T. Jin, Z.Q. Hu, H.U. Hong, B.G. Choi, I.S. Kim, and C.Y. Jo: *Philos. Mag. Lett.*, 2012, vol. 92, pp. 556–62.
57. J. Brenneman, J. Wei, Z. Sun, L. Liu, G. Zou, and Y. Zhou: *Corros. Sci.*, 2015, vol. 100, pp. 267–74.
58. N. Birks, G.H. Meier, and F.S. Pettit: *Introduction to the High Temperature Oxidation of Metals*, Cambridge University Press, Cambridge, 2006.
59. J. Chapovaloff, F. Rouillard, K. Wolski, and M. Pijolat: *Corros. Sci.*, 2013, vol. 69, pp. 31–42.
60. D.A. Jones: *Principles and Prevention of Corrosion*, Prentice Hall, Upper Saddle River, NY, 1996, pp. 168–98.
61. S.C. Tsai, A.M. Huntz, C. Dolin, and C. Monty: *Radiat. Effects Defects Solids*, 1995, vol. 137, pp. 285–90.
62. A.C.S. Sabioni, A.M. Huntz, F. da Silva, and F. Jomard: *Mater. Sci. Eng., A*, 2005, vol. 392, pp. 254–61.

**Publisher's Note** Springer Nature remains neutral with regard to jurisdictional claims in published maps and institutional affiliations.